RSC Advances

ROYAL SOCIETY OF CHEMISTRY

www.rsc.org/advances

Journal Name

ARTICLE

Near-infrared down-conversion in Er^{3+}-Yb^{3+} co-doped transparent nanostructured glass ceramics for crystalline silicon solar cells

Received 00th January 20xx,
Accepted 00th January 20xx

DOI: 10.1039/x0xx00000x

www.rsc.org/

Yuping Tai [a,c], Hanying Wang [b], Hui Wang [a, b, *], Jintao Bai [b, *]

A two-step energy transfer was achieved in Er^{3+}-Yb^{3+} co-doped transparent glass ceramics containing CaF_2 nanocrystals, which involved down-conversion of an absorbed visible photon to two emitted near-infrared photons. Therefore, the Yb^{3+} emission centered at 980 nm was efficiently enhanced and responded the strongest absorption of crystalline silicon solar cells. The mechanisms of the two-step energy transfer mechanism were verified based on spectra and lifetime measurements, and the maximal energy transfer efficiency and corresponding quantum yield were obtained as high as 75.3% and 150.6%, respectively. As a result, the near-infrared quantum cutting transparent glass ceramics will open a route to enhance the energy efficiency of the silicon solar cells.

[a] Key Laboratory of Synthetic and Natural Functional Molecule Chemistry (Ministry of Education), College of Chemistry and Materials Science, Northwest University, Xi'an 710069, P. R. China
[b] National Key Laboratory of Photoelectric Technology and Functional Materials (Culture Base), National Photoelectric Technology and Functional Materials and Application of International Science and Technology Cooperation Base, Institute of Photonics & Photon-Technology, Northwest University, Xi'an 710069, P. R. China
[c] School of Chemical Engineering & Pharmaceutics, Henan University of Science & Technology, Luoyang, 471023, P. R. China

*E-mail address: huiwang@nwu.edu.cn (Hui Wang) Tel.: +86 029 88363115
fax: +86 029 88302571
*E-mail address: baijt@nwu.edu.cn (Jintao Bai) Tel.: +86 029 88363115
fax: +86 029 88302571

DOI: 10.1039/x0xx00000x

Introduction

Crystalline silicon (c-Si) solar cells, which are extensively used in everyday life, have been particularly appealing. [1-2] However, great parts of solar energy was dissipated during the photovoltaic process owing to the thermalization of charge carriers whose energy exceeds the c-Si energy gap (E_g=1.12 eV), thus significantly limiting the conversion efficiency of solar cells.[3] Adapting the solar spectrum through down-conversion (DC) is an optimal scheme to reduce the energy loss caused by the thermalization, which involves the conversion of one ultraviolet (UV)-visible photon into two near-infrared (NIR) photons. [4-6] Recently, NIR DC in RE^{3+}/Yb^{3+} (RE=Tb, [7-9] Pr, [8,10,11] Tm, [8,10,12,13] Ce, [14-15] and Eu[16,17]) co-doped systems have been intensively investigated, on which excites RE^{3+} with a UV or visible photon and emits two NIR photons ~980 nm by Yb^{3+} that can be efficiently absorbed by c-Si solar cells through an DC process.

However, most of the DC between RE^{3+} and Yb^{3+} is achieved via a one-step cooperative energy transfer (ET) process, during which the system exhibits low emission intensity owing to concentration quenching and low energy transfer efficiency (ETE) between RE^{3+} and Yb^{3+}. [12,18-19] For more efficient DC, a two-step ET mechanism has been presented for Nd^{3+}-Yb^{3+},[20] Pr^{3+}-Yb^{3+},[21] and Er^{3+}-Yb^{3+} [22] lanthanide ion couples (to our knowledge). This two-step DC energy transfer is effective only when the donor has a suitable intermediate state to assist the sequential energy transfer to the acceptor. Herein we focus on the Er^{3+}-Yb^{3+} couple, which may suit for this condition ($^4I_{11/2}$ for Er^{3+}). Nevertheless, efficient DC by a two-step process cannot be easily implemented for the Er^{3+}-Yb^{3+} co-doped system due to the fast multi-photon relaxation from the $^4F_{7/2}$ level. [23] Some work has been performed for Er^{3+}-Yb^{3+} co-doped halides with low photon energy, but limit their applications because of poor thermal stability and adverse light scattering. [22, 24]

Recently, oxyfluoride glass ceramics (GCs) have attracted great attentions because of their low phonon energy and high chemical and mechanical stability, [25-27] which can suppress multi-photon relaxation processes between adjacent energy levels in Er^{3+} and enable efficient two-step ET from the $^4F_{7/2}$ level of Er^{3+}. Therefore, nanostructured GCs have been chosen as the host for Er^{3+}-Yb^{3+} couple to compensate for the shortcoming of the aforementioned hosts in our report. In addition, the evidence for the two-step ET process between the Er^{3+} and Yb^{3+} ions is presented based on spectra and lifetime measurements of Er^{3+}-Yb^{3+} co-doped GCs. Cross relaxation (CR) takes parts in the first ET step, leading to Er^{3+} populate in the $^4I_{11/2}$ level and Yb^{3+} in the $^2F_{5/2}$ state. After that, Er^{3+} will transfer another part of energy to Yb^{3+} via directly ET process in the second step. Both of the steps result in a NIR photon due to Yb^{3+} $^2F_{5/2}\rightarrow{}^2F_{7/2}$ transition. Finally, the calculated energy transfer efficiency (ETE) and the quantum yield (QY) of nanostructured GCs were as high as 75.3% and 150.6%, respectively. Therefore, the Er^{3+}-Yb^{3+} co-doped transparent nanostructured GCs make it possible to enhance the efficiency of c-Si solar cells as a DC layer.

Experimental

Synthesis of oxyfluoride GCs

The precursor oxyfluoride glass was prepared by the conventional melt-quenching method that uses high-purity reagent powders. The composition of the host precursor glass was $45SiO_2$-$15Al_2O_3$-20LiF-$20CaF_2$ in mol%. For each batch, about 20 g of mixed original materials were melted in a covered corundum crucible in a dry argon atmosphere at 1500 °C for 1 h, and then cast into a brass mold to form the precursor glass (PG). RE^{3+} were introduced in the form of Er_2O_3 and Yb_2O_3. The Er^{3+} concentration was fixed at 0.5 mol%, while the Yb^{3+} concentrations were set to 0, ,0.5, 1.0, 2.0,

and 5.0 mol%. The PG samples were subsequently heat-treated at 580 °C for 12 h to obtain GCs through crystallization. The GCs doped with different RE^{3+} concentration were donated as GC0, GC1, GC2, GC3 and GC4, respectively.

Materials Characterization

To confirm the crystallization phase of oxyfluoride glass, X-ray diffraction (XRD) analysis was performed by using a D/Max-3C diffractometer with Cu Kα radiation (1.5405 Å, 40 kV, 60 mA). The sizes and shapes of the glass nanocrystals were characterized by using high resolution transmission electron microscope (HRTEM, JEM2100). The visible-NIR absorption spectra were measured by using a Perkin-Elmer UV/vis/NIR Lambda 900 spectrophotometer. The excitation spectra and the emission spectra both in the visible and NIR regions, were recorded on an FLSP920 spectrofluorometer (Edinburgh Instruments, Britain). The emission and excitation measurements were performed by using a 450 W Xe lamp as the excitation source with the detector changing. The decay curves for the Er^{3+} 486 nm and 948 nm emissions upon 460 nm excitation were both recorded by using a μF900 pulse Xenon lamp.

Results and discussion

Structure behaviour

The XRD patterns of PG and GC are shown in Fig. 1 (a). The curve for the PG sample exhibits representative broad humps, indicating the material's amorphous structure. After thermally treating at 580 °C for 12 h, the characteristic diffraction peaks are observed at the 2θ angles of 28.21°, 47.01°, and 55.81°, confirming the orthorhombic CaF_2 (JCPDS 35-0816). The nanocrystal size is evaluated to be 10 nm by using the Scherrer formula. According to TEM micrograph in Fig. 1(b) and scanning transmission electron microscope (STEM) image in Fig. 1(c), it can be seen clearly that the nanoparticles sized at 8-10 nm distribute homogeneously in the glass matrix that is a good accordance with XRD result. Meanwhile, the high resolution TEM (HRTEM) image of individual CaF_2 nanocrystal is shown in Fig. 1 (d). The measured lattice spacing is 0.32 nm, which can be well-corresponded with the D-spacing value of (111) lattice plane of orthorhombic CaF_2, and the result is consistent with XRD patterns in Fig.1(a).

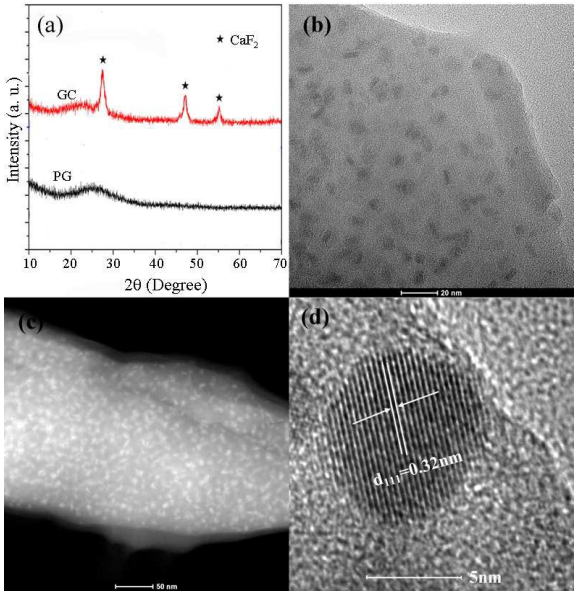

Fig.1 (a) XRD curves of PG and GC; (b) TEM micrograph of GC containing $0.5Eu^{2+}/0.5Yb^{3+}$:CaF_2 (GC1); (c) STEM micrograph of GC containing $0.5Eu^{2+}/0.5Yb^{3+}$:CaF_2 (GC1) (d) HRTEM image of individual nanocrystal.

Optical properties

The absorption spectra of the Er^{3+} single-doped (GC0)and Er^{3+}-Yb^{3+} co-doped containing $0.5Eu^{2+}/0.5Yb^{3+}$:CaF_2 (GC1) samples are presented in Fig. 2. The UV absorption edge that limits the glass transparency at shorter wavelengths is caused by the electronic transitions in the host glass. [20] It can be seen in Fig. 2, the observed peaks in the absorption spectrum of the GC0 are centered at 400, 460, 488, 520, 543, 650, 796, 948, and 1520 nm; these peaks were

ascribed to the absorption transitions from the $^4I_{15/2}$ ground state to every excited state of the Er^{3+} ion, including the $^2H_{9/2}$, $^4F_{5/2}$, $^4F_{7/2}$, $^2H_{11/2}$, $^4S_{3/2}$, $^4F_{9/2}$, $^4I_{9/2}$, $^4I_{11/2}$, and $^4I_{13/2}$, respectively. With the addition of Yb^{3+} ions (GC1), the peak wavelengths of all absorption bands were almost identical for GC0 sample, while the absorption band at ~980 nm became wider and stronger owing to the overlap between the Yb^{3+} $^2F_{7/2}$-$^2F_{5/2}$ and Er^{3+} $^4I_{15/2}$-$^4I_{11/2}$ transitions.

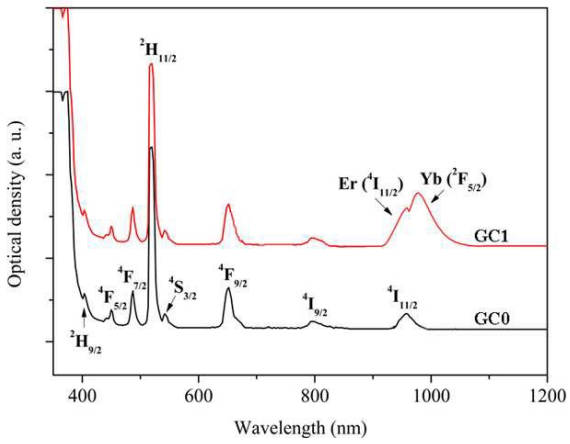

Fig.2 Absorption spectra of Er^{3+} single-doped (GC0) and Er^{3+}-Yb^{3+} co-doped GC containing $0.5Eu^{2+}/0.5Yb^{3+}$:CaF_2 (GC1).

Luminescence of Er^{3+} single doped and Er^{3+}-Yb^{3+} co-doped GCs

The photoluminescence excitation (PLE) and photoluminescence (PL) spectra in the GCs were measured to investigate whether the ET occurred from Er^{3+} to Yb^{3+}. It can be seen clearly that in the PLE spectra of Fig. 3(a) and (b), sharp excitation bands peaked at 460 nm corresponding to Er^{3+}: $^4I_{15/2}$→$^4F_{5/2}$ transition were recorded by monitoring both the Er^{3+}: $^4F_{7/2}$→$^4I_{15/2}$ transition at 486 nm and the Yb^{3+}: $^2F_{5/2}$→$^2F_{7/2}$ transition at 980 nm, verifying the existence of ET from Er^{3+} to Yb^{3+}. Furthermore, in the PL spectra of Fig.3 (c), a series of sharp emission peaks in the visible-NIR region are observed on the 460 nm excitation and decrease monotonously with the increasing of Yb^{3+} concentration, while the intensity of Yb^{3+} 980 nm emissions increases greatly simultaneously, which further elucidates the ET process from Er^{3+} to Yb^{3+}. However, as the concentration of Yb^{3+} increases from 2 mol% to 5 mol%, the emission intensity of Yb^{3+} at 980 nm becomes weaker than that of GC3, revealing the occurrence of cross-relaxation between the Yb^{3+} ions with increasing the Yb^{3+} concentration and reduced luminescence yield.

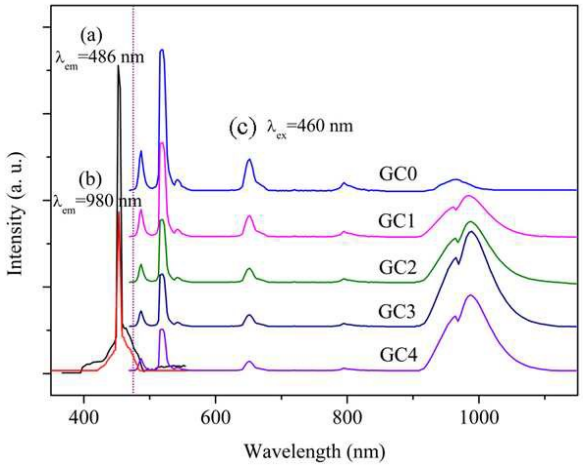

Fig.3 (a) PLE spectrum monitored by the Er^{3+}: $^4F_{7/2}$→$^4I_{15/2}$ emission (486 nm) and (b) the Yb^{3+}:$^2F_{5/2}$→$^2F_{7/2}$ emission (980 nm) in the GCs; (c) PL spectra of Er^{3+} in the GCs with different Yb^{3+} concentrations on excitation at 460 nm.

Mechanisms of ET from Er^{3+}: $^4F_{7/2}$ to Yb^{3+} in Pr^{3+}-Yb^{3+} co-doped GCs

In order to further testify the ET mechanism of DC, the photoluminescence spectra from 900-1100 nm from GC0 to GC4 are demonstrated in Fig. 4 (a). The emission spectra centered at 980 nm from GC1 to GC4 can be decomposed two independent peaks according to Gaussian deconvolution, which are ascribed to the Er^{3+}:$^4I_{11/2}$→$^4I_{15/2}$ (948 nm) and Yb^{3+}:$^2F_{5/2}$→$^2F_{7/2}$ (980 nm) transitions, respectively. In Fig. 4 (b), the emission spectra of Er^{3+} 948nm have been normalized by the intensity of Er^{3+}:$^4F_{9/2}$→$^4I_{15/2}$ (650 nm), and the latter does not participate in the ET process. The result shows

that the relative emission intensities of Er^{3+} 948 nm to 650 nm increase obviously with increasing Yb^{3+} concentrations.

According to above analysis of Figs.4 (a) and (b), the conclusion can be drawn as below. First, the emission intensities of Er^{3+} 948 nm increase gradually from GC0 to GC4 due to more photons populate on the $^4I_{11/2}$ energy level, subsequently, the emission intensities of Yb^{3+} are enhanced except the concentration quenching in GC4. The result make it possible of cross relaxation (CR) from Er^{3+}: $^4F_{7/2}$ to Yb^{3+}: $^2F_{7/2}$. Second, it is also possible that the Er^{3+} $^4F_{7/2}$ state transfers all the excitation energy directly to Yb^{3+}. However, direct ET will only populate $^2F_{5/2}$ state of Yb^{3+} and can not influence on the change of relative intensities of Er^{3+} $^4I_{11/2}$. While for CR, it will fill the excited states of Yb^{3+} and simultaneously increase the population of the Er^{3+} $^4I_{11/2}$ state with Yb^{3+} concentrations increased. Therefore, the increase of the relative intensities of Er^{3+} 948 nm to 650 nm should be owned to CR: Er^{3+} ($^4F_{7/2}$→$^4I_{11/2}$) - Yb^{3+}($^2F_{7/2}$→$^2F_{5/2}$), and the CR from Er^{3+} $^4F_{7/2}$ to Yb^{3+} $^2F_{7/2}$ dominates the first-step ET process.

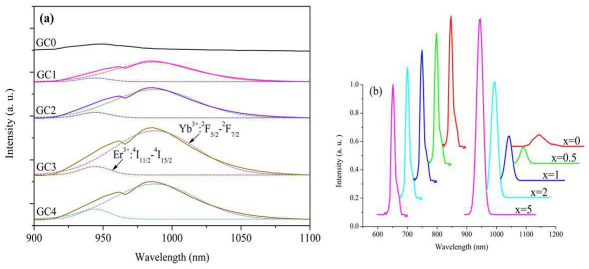

Fig. 4 (a) The photoluminescence (PL) spectra between 900-1100 nm in GCs and corresponding Gaussian deconvolution; (b) the change of relative emission intensity of Er^{3+} 948 nm (normalized by the intensities of $^4F_{9/2}$→ $^4I_{15/2}$ emissions).

Mechanisms of ET from Er^{3+}: $^4I_{11/2}$ to Yb^{3+} in Er^{3+}-Yb^{3+} co-doped GCs

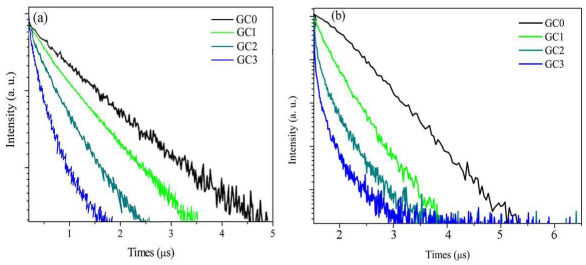

Fig.5 Decay curves of (a) Er^{3+}:$^4F_{7/2}$→$^4I_{11/2}$ transition (486 nm) (b) Er^{3+}:$^4I_{11/2}$→$^4I_{15/2}$ transition (948 nm) under 460 nm excitation.

In order to determine the second-step ET mechanism between Er^{3+} and Yb^{3+}, the typical luminescent dynamics of Er^{3+} $^4F_{7/2}$ and $^4I_{11/2}$ emissions in GCs are plotted in Figs. 5. Fig. 5(b) displays the decay curves of the Er^{3+} $^4I_{11/2}$ state, it can be seen that the Er^{3+} single doped GC shows a nearly single exponential decay. While for Er^{3+}-Yb^{3+} co-doped GCs, the decay curves deviate from single exponentials obviously with the increasing of Yb^{3+} concentration. Since the Er^{3+} concentration is fixed to 0.5 mol % in the four different GCs samples, the decrease of the lifetime should not be ascribed to the concentration quench of Er^{3+} but to direct ET from Er^{3+} $^4I_{11/2}$ to Yb^{3+} $^2F_{5/2}$, which indicates that a part of energy of the Er^{3+} $^4I_{11/2}$ is transferred to Yb^{3+} instead of being emitted in the Er^{3+}:$^4I_{11/2}$-$^4I_{15/2}$ transition completely. However, the rise component can not be observed that may be the depopulation process of $^4I_{11/2}$ state too fast. Therefore, the directly ET from Er^{3+} $^4I_{11/2}$ to Yb^{3+} $^2F_{5/2}$ is convinced as the second-step ET process according to Fig. 5(b).

Fig. 5 (a) is corresponding to the luminescence decay curves of the Er^{3+} $^4F_{7/2}$ state. It can be seen clearly that the lifetime of Er^{3+} $^4F_{7/2}$ (486 nm emission) decreases rapidly, which can be explained by the introduction of an extra relaxation pathway (CR ET process from Er^{3+} $^4F_{7/2}$ to Yb^{3+} $^2F_{5/2}$, testified as above). The

mean lifetime τ_m of 486 nm emission upon 460 nm excitation is calculated as follows:

$$\tau_m = \int_{t_0}^{\infty} [I(t)/I_0]dt$$

where I(t) is the luminescence intensity, and I_0 is the maximal value of I(t) that occurs at the time t_0. And the ETE is defined as the ratio of the number of donors that are depopulated by the ET to the acceptors over the total number of excited donors. The overall theoretical ETE for the GC samples can be calculated by using the following equation:

$$\eta_{ETE,xYb^{3+}} = 1 - \frac{\int I_{x\%,Yb^{3+}} dt}{\int I_{0\%,Yb^{3+}} dt}$$

As shown in Fig. 6, the τ_m and ETE are plotted vs. the concentration of Yb^{3+} ions, for GC0 to GC3. The lifetime decreased from 0.78 μs to 0.62 μs with increasing Yb^{3+} content from 0 mol% to 2 mol%, while the ETE increased to 75.3% with x=2 mol% composition of Yb^{3+} content.

In addition, the QY of Yb^{3+} is related to η_{ETE} as follows:

$$QY = 2\eta_{Yb}\eta_{ETE}$$

where η_{Yb} is the quantum emission efficiency of Yb^{3+}, which is usually about 100% owing to a low multi-photon relaxation rate and large energy gap between the $^2F_{7/2}$ and $^2F_{5/2}$ energy states.[28] The corresponding QY for the GC1, GC2, and GC3 were 70.2%, 136.6%, and 150.6%, respectively.

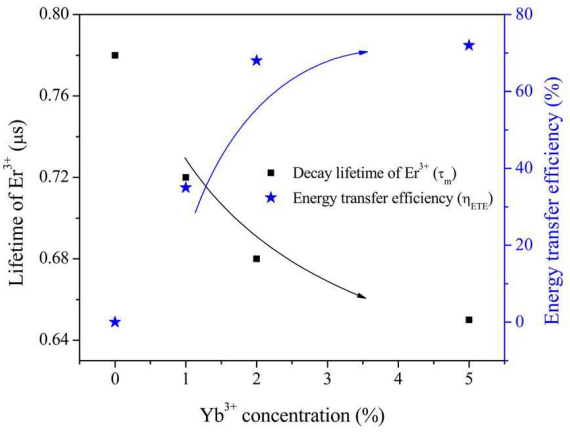

Fig.6 The mean decay lifetimes of the Er^{3+}:$^4F_{7/2}$→$^4I_{11/2}$ transition and ETE between the Er^{3+} and Yb^{3+} as a function of Yb^{3+} concentrations in GC0 to GC3.

The two-step ET mechanism

In Fig.7, the energy levels of Er^{3+} and Yb^{3+} are schematically illustrated, and a possible DC mechanism is also proposed for explaining the two-step ET between Er^{3+} and Yb^{3+}, as shown in Fig. 7. When Er^{3+} is excited into the $^4F_{5/2}$ state upon the 460 nm excitation and subsequently relaxes to the $^4F_{7/2}$ state, the $^4F_{7/2}$ state depopulates through a two-step sequential ET from Er^{3+} to Yb^{3+}, with Er^{3+}:$^4I_{11/2}$ acting as the intermediate state. In the first step (indicated by ①), a part of the Er^{3+} energy is transferred to Yb^{3+} according to the CR: Er^{3+}:$^4F_{7/2}$ + Yb^{3+}:$^2F_{7/2}$→Er^{3+}:$^4I_{11/2}$ + Yb^{3+}:$^2F_{5/2}$, the first NIR photon is acquired and Er^{3+} is still in the excited state $^4I_{11/2}$. In the second step (indicated by ②), another part energy of Er^{3+} is transferred to the second Yb^{3+} ion according to directly ET process and the second NIR photon is emitted, which is shown as Er^{3+}:$^4I_{11/2}$ + Yb^{3+}:$^2F_{7/2}$→Er^{3+}:$^4I_{15/2}$ + Yb^{3+}:$^2F_{5/2}$. Meanwhile, the emission of the Er^{3+}:$^4I_{11/2}$-$^4I_{15/2}$ transition may be occurred and acquired another NIR photon((indicated by ③).

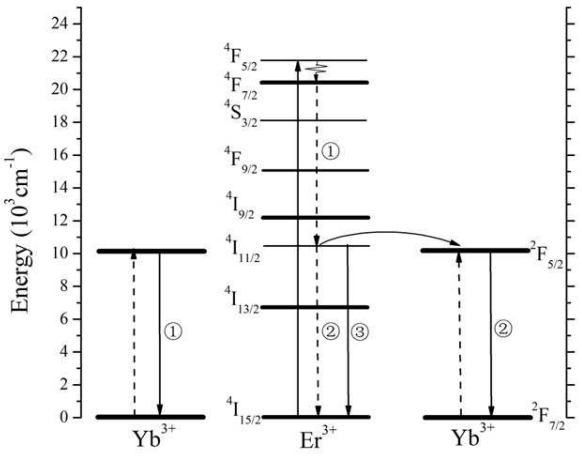

Fig. 7 Schematic energy level diagram of Er^{3+}-Yb^{3+} co-doped GCs, showing the two-step ET mechanism for the NIR emission under 460 nm excitation.

Conclusions

In summary, the Er^{3+}/Yb^{3+} co-doped GCs containing CaF_2 nanocrystals were obtained, and the efficient NIR DC took place by two-step ET process that was verified experimentally. The maximal ETE and QY values were estimated to be as high as 75.3% and 150.6%, respectively. According to the ET process, one visible photon can be converted into two NIR photons that can be efficiently absorbed by c-Si solar cells. Furthermore, GCs are advantageous owing to their higher thermal stability, transparency and low photon energy, which can adequately utilize the solar spectrum and increase the ETE of Er^{3+}-Yb^{3+} couple. Therefore, the Er^{3+}-Yb^{3+} co-doped GCs have a potential application as a DC layer to improve the conversion efficiency of c-Si solar cells.

Acknowledgements

This work was supported by National Hi-Tech Research and Development Program (863) Key Project of China (No. 2012AA050301-SQ2011 GX01D01292), and Xi'an Industrial Technology Innovation Project-technology transfer promoting program (No.CX1242,CXY1123-5,CX12182-2,CX12182-3,CXY1421).

Notes and references

1 M. Ye and X. Wang, *Chin. Opt. Lett.* ,2014, **12**, 053501 .

2 J. Fan, B. Jia and M. Gu, *Photon. Res.*, 2014, **2,** 111-120 .

3 C. Strümpel, M. McCann, G. Beaucarne, V. Arkhipov, A. Slaoui, V. Švrček, C. del Cañizo and I. Tobias, *Sol. Energy Mater. Sol. Cells,* 2007, **91**, 238-249.

4 Trupke T, Green M A and Würfel P, *J. Appl. Phys.,* 2002, **92**, 1668-1674 .

5 B. S. Richards, *Sol. Energy Mater. Sol. Cells,* 2006, **90**, 1189-1207.

6 B. S. Richards, *Sol. Energy Mater. Sol. Cells,* 2006, **90**, 2329-2337.

7 S. Ye, B. Zhu, J. Chen, J. Luo and J. Qiu, *Appl. Phys. Lett.*, 2008, **92,** 141112.

8 Q. Y. Zhang, G. F. Yang and Z. H. Jiang, *Appl. Phys. Lett.,* 2007, **91,** 051903.

9 X. Liu, S. Ye, Y. Qiao, G. Dong, B. Zhu, D. Chen, G. Lakshminarayana and J. Qiu, *Appl. Phys. B,* 2009, **96,** 51-55.

10 G. Lakshminarayana and J. Qiu, *J. Alloys. Compd.,* 2009, **481,** 582-589.

11 Y. Xu, X. Zhang, S. Dai, B. Fan, H. Ma, J. I. Adam, J. Ren and G. Chen, *J. Phys. Chem. C*, 2011, **115,** 13056-13062 .

12 L. Xie, Y. Wang and H. Zhang, *Appl. Phys. Lett.,* 2009, **94** , 061905.

13 S. Ye, B. Zhu, J. Luo, J. Chen, G. Lakshminarayana and J. Qiu, *Opt. Exp.*, 2008, **16**, 8989-8994.

14 X. Liu, Y. Teng, Y. Zhuang, J. Xie, Y. Qiao, G. Dong, D. Chen and J. Qiu, *Opt. Lett.,* 2009, **34,** 3565-3567.

15 H. Lin, S. Zhou, H. Teng, Y. Li and W. Li, *J. Appl. Phys.,* 2010, **107** 043107.

16 Y. Tai, G. Zheng, H. Wang and J. Bai, *J. Solid State Chem.*, 2015, **226**, 250-254.

17 K. Biswas, S. Balaji, D. Ghosh, A. D. Sontakke and K. Annapurna, *J. Alloys. Compd.,* 2014, **608**, 266-271.

18 Q. Y. Zhang, C. H. Yang, Z. H. Jiang and X. H. Ji, *Appl. Phys. Lett.*, 2007, **90,** 061914 .

19 D. Q. Chen, Y. L. Yu, Y. S. Wang and P. Huang, *J. Phys. Chem. C,* 2009, **113**, 6406-6410.

20 D. Chen, Y. Yu, H. Lin, P. Huang, Z. Shan and Y. Wang, *Opt. Lett.*, 2010, **35,** 220-222.

21 B. M. van der Ende, L. Aarts and A. Meijerink, *Adv. Mater.,* 2009, **21 ,** 3073-3077.

22 J. J. Eilers, D. Biner, J. T. van Wijngaarden, K. Krämer, H.-U. Güdel and A. Meijerink, *Appl. Phys. Lett.*, 2010, **96,** 151106.

23 L. Aarts, B. M. van der Ende and A. Meijerink, *J. Appl. Phys.,* 2009, **106,** 023522.

24 S. R. Lüthi, H. U. Güdel and M. P. Hehlen, *J. Chem. Phys.,* 1999 ,**110 ,** 12033-12043.

25 L. H. Huang, T. Yamashita, R. Jose, Y. Arai, T. Suzuki, and Y. Ohishi, *Appl. Phys. Lett.,* 2007, **90,** 131116.

26 L. H. Huang, G. S. Qin, Y. Arai, R. Jose, T. Suzuki, Y. Ohishi, T. Yamashita, and Y. Akimoto, *J. Appl. Phys.,* 2007, **102**, 093506.

27 D. Q. Chen, Y. S. Wang, Y. L. Yu, F. Liu, and P. Huang, *Opt. Lett.* , 2007, **32**, 3068-3070.

28 J. Zhou, Y. Zhuang, S. Ye, Y. Teng and G. Lin, *Appl. Phys. Lett.,* 2009, **95**, 141101.